

EES Solar

Accepted Manuscript

This article can be cited before page numbers have been issued, to do this please use: F. Zarotti, E. Magliano, S. K. Podapangi, F. Trezzini, E. Ghavidel, V. Raglione, M. Di Giovannantonio, F. Di Giacomo, A. coati, R. Felici and A. Di Carlo, *EES Sol.*, 2026, DOI: 10.1039/D5EL00193E.



This is an Accepted Manuscript, which has been through the Royal Society of Chemistry peer review process and has been accepted for publication.

Accepted Manuscripts are published online shortly after acceptance, before technical editing, formatting and proof reading. Using this free service, authors can make their results available to the community, in citable form, before we publish the edited article. We will replace this Accepted Manuscript with the edited and formatted Advance Article as soon as it is available.

You can find more information about Accepted Manuscripts in the [Information for Authors](#).

Please note that technical editing may introduce minor changes to the text and/or graphics, which may alter content. The journal's standard [Terms & Conditions](#) and the [Ethical guidelines](#) still apply. In no event shall the Royal Society of Chemistry be held responsible for any errors or omissions in this Accepted Manuscript or any consequences arising from the use of any information it contains.

Broader context

Formamidinium lead iodide (FAPbI₃) continues to attract significant interest as a highly promising perovskite absorber for next-generation photovoltaics, yet its full potential remains constrained by challenges in vacuum-based fabrication. Thermal co-evaporation, a technique well suited for industrial scaling, has been particularly difficult for FAPbI₃ due to phase instability and decomposition of organic iodide precursors. As the field increasingly moves toward solvent-free and highly controlled deposition methods, developing reliable approaches to evaporated FAPbI₃ is both timely and essential.

This work addresses these limitations by introducing an additive-free co-evaporation strategy that employs multiple FAI sources, mitigating thermal degradation and enabling the growth of high-quality, thick films. The study further elucidates the critical influence of substrate temperature and intermediate annealing on phase purity and crystallization, offering insights into controlling α -phase formation. By comparing MeO-2PACz and PTAA hole transport layers and demonstrating efficient *p-i-n* devices, the results advance the technological feasibility of vacuum-processed FAPbI₃ photovoltaics.

By identifying processing windows that yield thick, uniform, and highly crystalline α -phase films, this work contributes to establishing vapor-phase deposition as a robust and industrially viable route for perovskite photovoltaics.



ARTICLE

Tailoring Crystallization Dynamics and Phase Evolution of Co-evaporated Pure α -FAPbI₃ for Enhanced Device Performance

Francesca Zarotti^{a,d,e,*}, Erica Magliano^{b,d}, Suresh Podapangi^a, Federico Trezzini^a, Elham Ghavidel^a, Venanzio Raglione^b, Marco Di Giovannantonio^b, Francesco Di Giacomo^{a,f}, Alessandro Coati^c, Roberto Felici^b, and Aldo Di Carlo^{a,b,*}

Received 00th January 20xx,
Accepted 00th January 20xx

DOI: 10.1039/x0xx00000x

Formamidinium lead iodide (FAPbI₃) is among the most promising perovskite composition for high-efficiency photovoltaics. However, its thermal co-evaporation remains technically challenging due to inherent phase instability and thermal decomposition of the organic precursors. In this work, we demonstrate an additive-free thermal co-evaporation of pure FAPbI₃, by sequentially employing multiple sources of formamidinium iodide (FAI). This strategy effectively mitigates process instabilities of FAI during prolonged evaporation, enabling the growth of thick perovskite films with improved morphology. Furthermore, we show that the introduction of an intermediate annealing step significantly enhances crystallization dynamics during thickness scaling, resulting in highly ordered and coherent film structures. A systematic investigation of substrate temperature during deposition highlights its crucial role on phase purity and crystallinity. Notably, films grown at 60 °C exhibit superior structural order and effective suppression of the undesired hexagonal non-perovskite phases, as confirmed by X-ray diffraction analysis. We also compare two widely used hole transport layers, MeO-2PACz and PTAA, and show that, although MeO-2PACz promotes α -phase formation, it poses challenges related to film morphology and processing reproducibility. Finally, devices employing PTAA in a $p-i-n$ architecture achieve a power conversion efficiency of 18.5% using pure, thermally evaporated FAPbI₃.

1. Introduction

Perovskite solar cells (PSCs) have emerged as a highly promising photovoltaic technology due to their optoelectronic properties, improved light absorption, direct and tunable bandgap, and high carrier mobility.^{1,2} Among the various perovskite compositions, formamidinium lead triiodide (FAPbI₃, or FAPI, chemical formula: CH(NH₂)₂PbI₃) stands out thanks to its optimal bandgap of approximately 1.48 eV, which closely matches

the optimal value predicted by the Shockley-Queisser limit for the maximum solar energy conversion efficiency.³ FAPbI₃ also exhibits enhanced thermal stability compared to other widely investigated hybrid metal halide perovskites (MHPs), such as MAPbI₃, attributed to the formamidinium proton being relatively inert and making it a more suitable candidate for long-term operational stability at elevated temperatures.^{4,5} Moreover, the compositional simplicity of FAPbI₃, consisting of a single A-site cation and a single halide, represents a significant advantage compared to alloyed perovskites incorporating multiple A-site cations (e.g., Cs⁺, MA⁺) or mixed halides (I⁻/Br⁻). Although compositional engineering through cation or halide mixing has been widely employed to enhance structural stability, it increases the chemical complexity, as well as the bandgap.⁶ Additionally, halide compositions are well known to be prone to halide segregation under thermal or light stress.^{7,8} Achieving and maintaining the photoactive α -phase of FAPbI₃ during crystallization and under operational conditions remains a critical challenge. In fact, while the black photoactive α -phase (cubic) exhibits excellent optoelectronic properties, it is thermodynamically metastable at room temperature and readily converts into the wide-bandgap (~2.4 eV) yellow δ -phase (hexagonal) during crystallization and under prolonged exposure to ambient conditions. This transformation is further

^aC.H.O.S.E. (Center for Hybrid and Organic Solar Energy), Electronic Engineering Department, University of Rome Tor Vergata, Via del Politecnico 1, 00118, Rome, Italy.

^bCNR – Istituto di Struttura della Materia (CNR-ISM), via Fosso del Cavaliere 100, 00133 Roma (Italy)

^cSynchrotron SOLEIL, L'Orme des Merisiers, Saint-Aubin, 91192 Gif sur Yvette, France

^dBoth authors contributed equally to this work.

Present addresses:

^e ENEA, Italian National Agency for New Technologies, Energy and Sustainable Economic Development, Via Enrico Fermi, 45, 00044 Frascati, Rome, Italy.

^f Solertix S.r.l., Via Eusebio Chini 15, 00147, Rome, Italy.

Supplementary Information available: [details of any supplementary information available should be included here]. See DOI: 10.1039/x0xx00000x



1 accelerated in the presence of moisture and at elevated
2 temperatures.^{9–12} This phase transition undermines device
3 efficiency and durability. Numerous stabilization
4 approaches, such as cation/ halide mixing or additive
5 engineering, have been proposed.^{13–22} However, these
6 solutions often come at the cost of increased complexity,
7 as well as causing bandgap widening, defect formation, or
8 inhomogeneous film morphology, ultimately limiting their
9 practical scalability.

10 Remarkable performance of pure α -FAPbI₃-based solar
11 cells has been enabled by a series of innovative
12 approaches aimed at improving phase stability and
13 optoelectronic quality.^{23,24} For instance, Huang *et al.*
14 employed hexafluorobenzene (HFB) to lower the chemical
15 potential of formamidinium iodide (FAI), effectively
16 slowing down its reaction with lead iodide (PbI₂). This
17 strategy helped suppress the formation of the undesired
18 δ -phase, which would otherwise compromise device
19 stability.²³ In a separate work, Cao *et al.* showed that the
20 incorporation of a triphenylamine (TPA)-functionalized
21 ligand significantly enhances charge transport in FAPbI₃
22 perovskite solar cells. This molecular engineering led to
23 improved film quality and boosted the efficiency of 2D/3D
24 FAPbI₃-based devices, with a champion power conversion
25 efficiency (PCE) of 25.7%.²⁴ These high performances were
26 all achieved using solution-based deposition techniques,
27 which remain the leading fabrication methods for PSCs.
28 This is largely attributed to the low cost and accessibility of
29 solution processing, which have enabled rapid
30 development of efficient synthesis and passivation
31 protocols.^{25,26} As a result, solution-processed perovskites,
32 including all various formulations, as well as pure FAPbI₃,
33 continue to lead the field of PSC development.

34 In contrast, thermal evaporation has received
35 comparatively less attention and lags behind in
36 efficiency.²⁵ The current record for vacuum-deposited
37 PSCs is 20.6% for a co-evaporated MAPbI₃-based device.²⁷
38 While vapor deposition offers significant advantages in
39 terms of scalability, reproducibility, and compatibility with
40 industrial processes,²⁸ its development has been hindered
41 by challenges related to the thermal evaporation of
42 organic salts due to their high-vapor pressure and volatile
43 behavior.^{29–32} Specifically, FAI presents a major challenge
44 due to its thermal instability and decomposition.^{32,33} As
45 shown by Kroll *et al.*, FAI tends to degrade at elevated
46 source temperatures, forming unwanted byproducts that
47 increase the background pressure inside the chamber.³²
48 This degradation not only reduces the amount of FAI that
49 successfully reaches the substrate, but also leads to a
50 stoichiometric imbalance in the resulting perovskite film.
51 Moreover, the development of thermally evaporated
52 FAPbI₃ has been further constrained by the absence of
53 well-defined additive engineering protocols compatible
54 with vacuum deposition processes, making it more
55 challenging to replicate the strategies adopted in solution-
56 based systems.

57 In this work, we demonstrate the additive-free thermal co-
58 evaporation of pure FAPbI₃ by sequentially employing
59 multiple FAI sources, rather than operating them in
60 parallel. Our strategy effectively circumvents the time-
61 dependent evolution of the FAI source during prolonged
62 evaporation and enables the growth of thick FAPI layers
63 overcoming difficulties in FAI control. Furthermore, we
64 demonstrate that introducing an intermediate annealing
65 step improves the crystallization dynamics when
66 increasing the perovskite thickness, leading to a more
67 coherent and better-ordered film structure. We further
68 investigate the impact of substrate temperature and
69 substrate nature on perovskite film formation and
70 properties.

71 The role of substrate temperature during co-evaporation
72 has been extensively studied for MAPbI₃, where the
73 substrate temperature strongly influences MAI adsorption
74 and thus final film morphology and stoichiometry.^{31,34–37}
75 However, the influence of temperature on FAI-based
76 compositions has received limited attention. Gil-Escrig *et al.*
77 conducted a systematic study on Cs_{0.2}FA_{0.8}Pb(I_{0.8}Br_{0.2})₃
78 showing that reduced FAI incorporation at elevated
79 temperatures can promote improved film morphology.³⁸
80 Building on this, we explore co-evaporated FAPI growth at
81 four different substrate temperatures (T_{sub}): -10 °C, 20 °C,
82 50 °C, and 60 °C. Structural and morphological
83 characterization reveals a clear evolution in crystallinity
84 and phase purity. Notably, GIXD analysis on films grown at
85 20 °C and 60 °C highlights that 60 °C promotes a higher
86 degree of crystalline order and effectively suppresses the
87 formation of undesired hexagonal phases.

88 As for the substrate nature, recent studies have
89 highlighted the significant role of the hole transport layer
90 (HTL) in influencing perovskite film growth during thermal
91 evaporation.^{39–43} In particular, unwashed [n]-phosphonic
92 acid carbazole (nPACz) layers promote FAI adsorption
93 through exposed phosphonic acid groups, which interact
94 strongly with iodide via hydrogen bonding.³⁹ This
95 interaction creates an energetic barrier that suppresses
96 the transformation of the photoactive α -FAPbI₃ phase into
97 the undesirable δ -phase, thereby kinetically stabilizing the
98 desired perovskite structure. The improved FAI adhesion
99 on nPACz surfaces allows for a lower FAI deposition rate to
100 achieve optimal stoichiometry and crystallinity, promoting
101 the formation of high-quality perovskite films. Conversely,
102 these same interactions between phosphonic acid and
103 hydrogen groups can become problematic for bromide-
104 containing compositions, as highlighted by Öz *et al.*⁴²
105 Castro-Méndez *et al.* further demonstrated that the
106 migration of excess phosphonic acid species during film
107 growth contributes positively to α -phase stabilization by
108 maintaining a steady supply of adsorbed organic
109 precursors at the growth front, thereby reducing the
110 energy barrier for crystallization and enhancing the FAI
111 adsorption rate.⁴⁰ Nevertheless, excess of nPACz



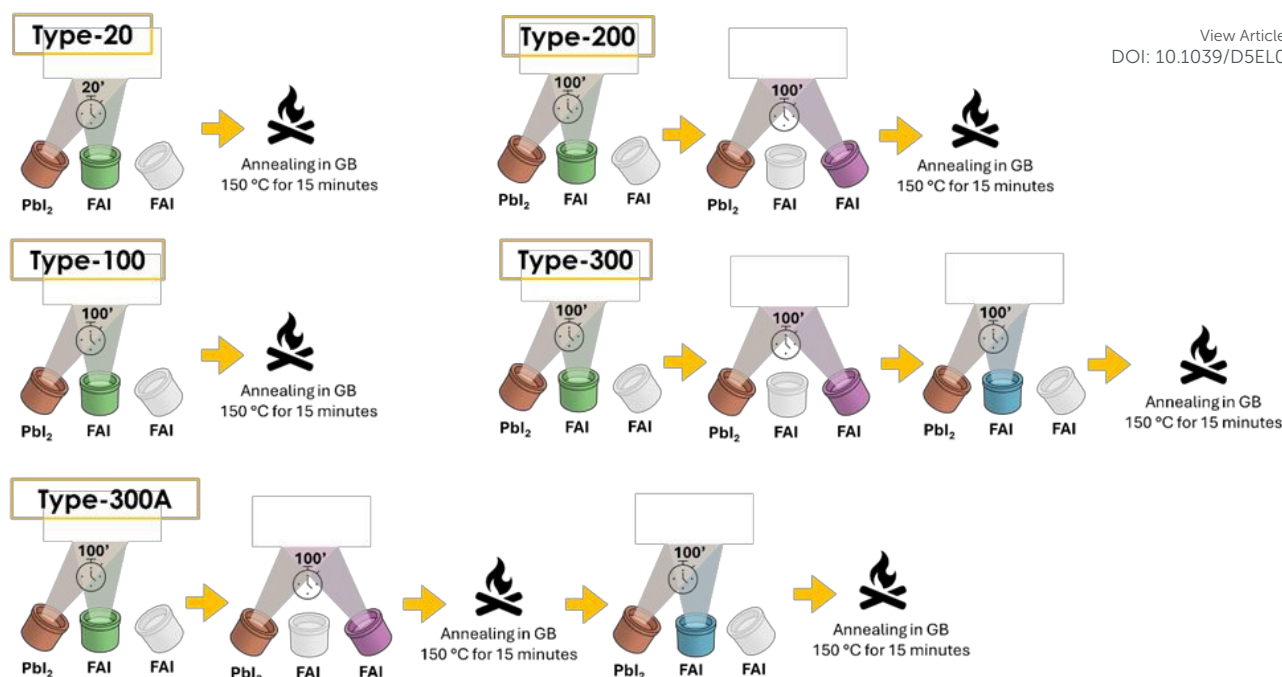


Figure 1: Schematics of different deposition processes of FAPbI₃, labelled as Type-20, Type-100, Type-200, Type-300, Type-300A.

1 molecules can negatively impact device performance by
 2 forming an insulating interfacial layer or inducing FAI
 3 excess, which may reduce open-circuit voltage (V_{OC}) and
 4 short-circuit current density (J_{SC}).^{39,41} To mitigate this, a
 5 mild rinsing step is sometimes employed, though it risks
 6 partial exposure of the underlying ITO and uncontrolled
 7 interfacial effects.

8 To clarify the influence of the underlying substrate on the
 9 crystallization behavior of co-evaporated FAPbI₃, we
 10 conducted a comparative study using [2-(3,6-Dimethoxy-
 11 9H-carbazol-9-yl)ethyl]phosphonic acid (MeO-2PACz) and
 12 Poly[bis(4-phenyl)(2,4,6-trimethylphenyl)amine] (PTAA) as
 13 HTLs. The results showed that MeO-2PACz more
 14 effectively promotes the formation of the photoactive α -
 15 FAPbI₃ phase and suppresses non-perovskite phases
 16 compared to PTAA. However, this advantage is
 17 counterbalanced by inferior film morphology and limited
 18 process reproducibility. Consequently, PTAA yielded
 19 superior device performance under the same growth
 20 conditions. By fine-tuning critical parameters - including
 21 deposition procedure, substrate temperature, and HTL -
 22 we achieved enhanced performance in a $p-i-n$
 23 architecture, reaching a power conversion efficiency of
 24 18.5% with thermally evaporated pure FAPbI₃. An
 25 impressive long-term stability is demonstrated in shelf life,
 26 and the final encapsulated device show a T_{80} (time in which
 27 the PCE reaches 80% of the initial PCE)⁴⁴ of 400 hours.

29 2. Results and discussion

30 We investigate the optimal process conditions and the
 31 effect of the substrate on the growth quality of FAPbI₃
 32 deposited by the co-evaporation of FAI and PbI₂.

33 The precursor quantities were measured and loaded into
 34 each crucible prior to every deposition run. To prevent FAI
 35 decomposition during evaporation, the source
 36 temperature was maintained at 210 °C. Higher
 37 temperatures were deliberately avoided to minimize the
 38 risk of carbonization or thermal degradation of FAI during
 39 the deposition process, as discussed in SI.^{32,33} Co-
 40 deposition started once the crucibles reached their target
 41 temperatures: 345 °C for PbI₂ and 210 °C for FAI (further
 42 details can be found in Experimental Section). The
 43 substrate temperature was regulated using a stainless
 44 steel holder cooled by a water-glycol mixture connected
 45 to an external temperature bath. Perovskite films were
 46 deposited at substrate temperatures ranging from -10 °C
 47 to 60 °C.

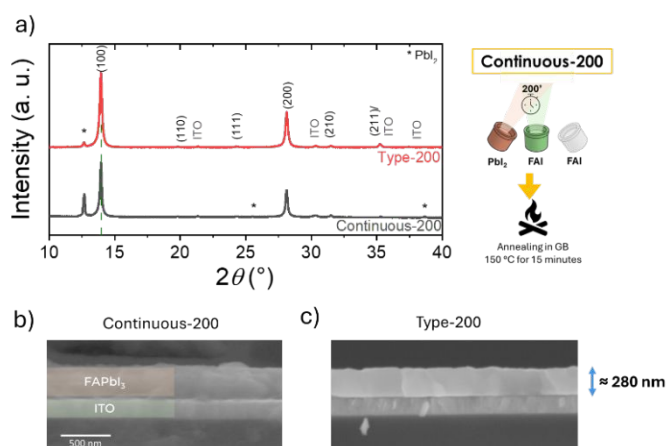


Figure 2: a) XRD spectra of FAPbI₃ deposited continuously for 200 min (Continuous-200) and Type-200 FAPbI₃ on glass/ITO/PTAA with substrate temperature set at 60 °C during co-evaporation process. A schematic of the Continuous-200 process is also shown on the right. b, c) Cross-section SEM images of the two perovskite types.



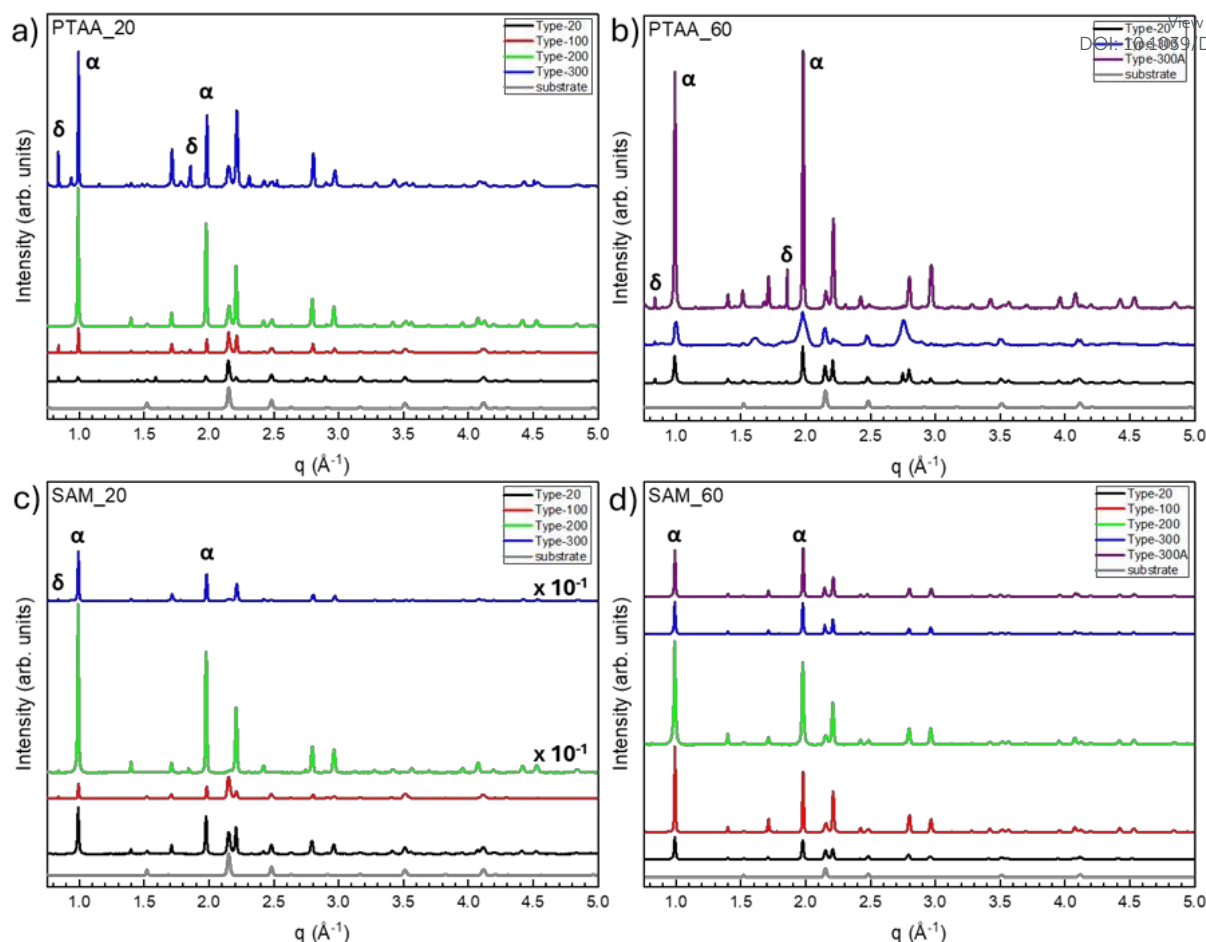


Figure 3: GIXD plots of FAPbI₃ films deposited on PTAA (top plots) and SAM (bottom plots) at substrate temperatures of 20 °C (left plots) and 60 °C (right plots). The perovskite was co-evaporated using different deposition procedures: Type-20 (black curve), Type-100 (red curve), Type-200 (green curve), and Type-300 (blue curve). Type-300A (purple curve) is also included for depositions at 60 °C on both PTAA and SAM. Substrate spectra are shown in grey as a reference.

Owing to the large impact of temperature on crystallization and morphology of co-evaporated FAPbI₃, we first explored the impact of substrate temperatures on deposition. A preliminary study was conducted by testing a range of possible substrate temperatures (−10°C, 20°C, 50°C, and 60°C) during a continuous co-deposition process of 120 min. XRD analysis (Figure S2) revealed enhanced crystallinity at 60°C, as indicated by the lowest full width at half maximum (FWHM) and highest intensity of the α-phase (100) peak, which is an evidence of a more ordered and crystalline structure. Notably, good crystallinity was also observed at 20°C. Based on these results, 20°C and 60°C were selected for further investigation using grazing-incidence X-ray diffraction (GIXD).

Studies of the structural properties of FAPbI₃ perovskite were conducted on different films deposited on two different hole transport layers (HTLs): MeO-2PACz, hereafter referred to as self-assembled monolayer (SAM), and PTAA. The abovementioned substrate temperatures of 20°C and 60°C were employed for both the HTLs under examination.

Multiple FAI sources were employed at different stages of the deposition to modulate the incorporation dynamics,

effectively preventing time-dependent changes in the FAI source under prolonged evaporation.

Films were deposited for varying durations (20, 100, 200, and 300 minutes) hereafter referred to as Type-20, Type-100, Type-200, and Type-300, respectively. In Type-200, two FAI sources were employed consecutively 100 minutes each, without breaking the vacuum.

Additionally, samples labelled with Type-300A underwent a two-step deposition process: an initial 200-minute deposition (Type-200) followed by annealing (150°C for 15 min), then an additional 100-minute deposition. A final annealing step at 150 °C for 15 min was always performed in order to promote the transition from δ-phase to α-phase (Figure S3-S4). A schematic of the different deposition processes is shown in Figure 1.

We initially tested perovskite fabrication using a continuous 200-minute FAPbI₃ evaporation process, without any FAI substitution or modification during vacuum deposition (Figure 2). This study was performed on glass/ITO/PTAA with substrate temperature of 60°C during co-evaporation. The sample prepared via continuous 200 minute FAPbI₃ evaporation (indicated as “Continuous-200”) exhibits a more pronounced PbI₂ peak, indicative of incomplete conversion, as compared to the



1 spectrum of Type-200 perovskite film. In contrast, the
 2 Type-200 sample displays a sharp and intense (100)
 3 perovskite peak along with a weaker PbI_2 signal, indicating
 4 more complete and uniform perovskite formation, as also
 5 verified by XRD analysis in ambient air over time (Figure
 6 S5). Notably, both the Type-200 and the Continuous-200
 7 deposition processes yield perovskite films with similar
 8 thicknesses (~ 280 nm, Figure 2), suggesting that the
 9 formed PbI_2 does not result from under conversion due to
 10 insufficient FAI precursor supply but rather from a
 11 different evaporation behavior of FAI.

12 To further investigate its behavior during prolonged
 13 evaporation, we performed $^1\text{H-NMR}$ measurements on FAI
 14 powder collected at different evaporation times (Figure
 15 S6). From the comparison of the $^1\text{H-NMR}$ spectra, the
 16 evaporation process appears to promote a progressive
 17 purification of FAI, as evidenced by the systematic increase
 18 in the $-\text{NH}_2$ peak intensity when extending the evaporation
 19 time from 20 to 200 minutes. However, the sample
 20 evaporated for 20 minutes exhibits a lower signal intensity
 21 compared to pristine FAI. This behavior may be attributed
 22 to the initial formation of byproducts (e.g., HI), which could
 23 induce peak broadening and consequently reduce the
 24 apparent signal intensity. Upon increasing the evaporation
 25 time, these byproducts are progressively removed, in
 26 agreement with literature reports³², resulting in a gradual
 27 sharpening and intensification of the $-\text{NH}_2$ peak.³³ We
 28 hypothesize that prolonged evaporation of FAI may lead to
 29 progressive physical and chemical changes in the precursor
 30 residue within the crucible, driven by the depletion of
 31 volatile species and alterations in the surface morphology
 32 of the FAI powder. These changes can, in turn, affect the
 33 stoichiometry and dynamics of the vapor phase.

34 To circumvent FAI instability over prolonged evaporation
 35 time, each FAI source was employed for a maximum of 100
 36 minutes. Therefore, for longer deposition processes (i.e.,
 37 Type-200, Type-300, Type-300A), FAI was introduced from
 38 different sources sequentially, rather than simultaneously,
 39 to further control the film composition and morphology.

40 The samples under investigation are indicated as
 41 "HTL_substrate temperature", e.g. PTAA_20 indicates the
 42 FAPbI_3 grown on PTAA with a substrate temperature of
 43 20°C during vacuum deposition. For each sample, a
 44 comprehensive peak and phase identification analysis was
 45 performed starting from spectra reported in Figure 3. The
 46 spectra were measured and normalized to the substrate
 47 reference peak to ensure consistent comparison.

48 Structurally, both the α -phase (cubic) and δ -phase
 49 (hexagonal) are present in the samples, except for SAM_60
 50 where only the α -phase is detected (Figure 3). In particular,
 51 the two most intense peaks are located at $q \approx 0.99 \text{ \AA}^{-1}$
 52 $[[100]]$ and $q \approx 1.98 \text{ \AA}^{-1}$ $[[200]]$ for the α -phase, and at $q \approx$
 53 0.84 \AA^{-1} $[[100]]$ and $q \approx 1.85 \text{ \AA}^{-1}$ $[[201]]$ for the δ -phase,
 54 with the single polytype 2H detected (Figure S7).

55 In the case of PTAA-based samples (Figure 3 - a,b),
 56 increasing the substrate temperature to 60°C enhances
 57 the formation of the photoactive α -cubic phase of FAPbI_3

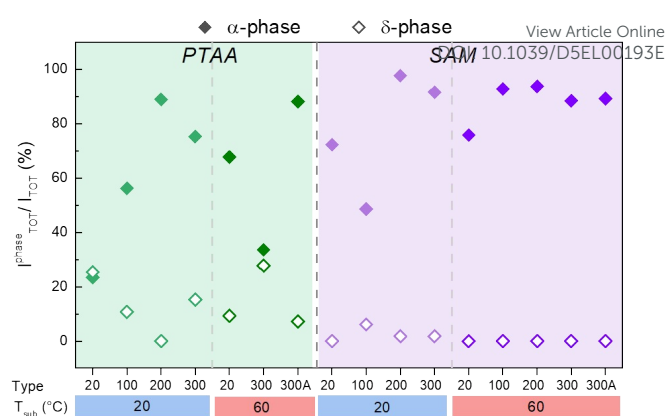


Figure 4: α - and δ -phase content expressed as the percentage ratio of total peak intensities for each phase over the sum of all peak intensities in the diffraction spectrum, shown for all samples.

58 while reducing the presence of hexagonal δ -phase
 59 impurities, compared to films deposited at 20°C . A similar
 60 trend is observed for samples deposited on SAM (Figure 3
 61 - c,d), where the promotion of the α -phase is even more
 62 pronounced. In particular, no δ -phase is detected at 60°C
 63 on SAM (Figure 3 - d), whereas at 20°C (Figure 3 - c), a
 64 weak δ -phase peak begins to emerge from the Type-100
 65 deposition condition onward.

66 Notably, the α -phase is present in all samples after only 20
 67 minutes of deposition, regardless of substrate type or
 68 temperature. In contrast, the δ -phase appears at this early
 69 stage exclusively in PTAA-based samples, indicating
 70 distinct interfacial interactions between the growing
 71 perovskite film and the underlying HTL. This suggests that
 72 the SAM layer is playing a templating role during
 73 nucleation, favoring the stabilization of the α -phase over
 74 the δ -phase. SAMs have previously been reported to
 75 significantly influence FAPbI_3 co-evaporation and growth
 76 dynamics, mainly due to the presence of the phosphonic
 77 acids, by promoting α -phase formation and suppressing
 78 phase impurities.^{39,40,45} Our observations are consistent
 79 with these reports, confirming that the presence of SAMs
 80 modulates crystallization pathways, ultimately favoring
 81 the formation of phase-pure α - FAPbI_3 films. In our case,
 82 since no post-deposition washing or surface treatment
 83 was performed after SAM application, it is likely that the
 84 layer is not limited to a compact monolayer. Instead, some
 85 unbound nPACz molecules may remain on the surface,
 86 exposing additional phosphonic acid functional groups.
 87 These exposed groups can interact with FAI during
 88 deposition, potentially enhancing its incorporation into
 89 the growing perovskite film. As reported by Feeney *et al.*,
 90 hydrogen bonding between surface iodide ions in the
 91 FAPbI_3 lattice and phosphonic acid groups of nPACz can
 92 introduce an energetic barrier that suppresses the
 93 transition from the photoactive α -phase to the non-
 94 perovskite δ -phase.³⁹ This interaction may contribute to
 95 the improved phase growth and formation observed in our
 96 SAM-based samples.



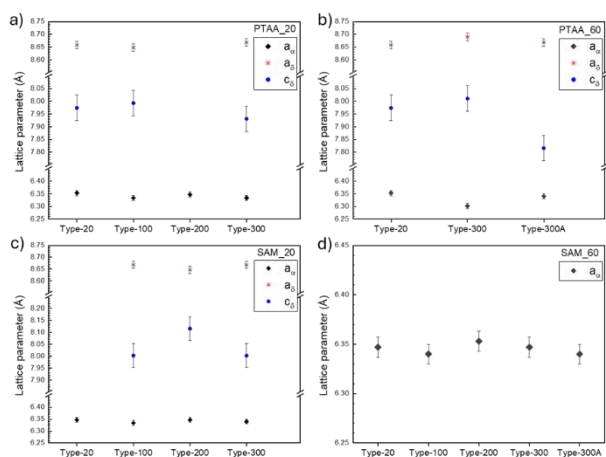


Figure 5: Lattice parameters estimated from diffraction analysis for FAPbI₃ films deposited on PTAA at substrate temperatures of (a) 20 °C and (b) 60 °C, and on SAM at (c) 20 °C. For each sample, the cubic lattice parameter a_{α} and the hexagonal parameters a_{δ} and c_{δ} are reported. In panel (d), corresponding to FAPbI₃ grown on SAM at 60 °C, only the a_{α} parameter is shown, as no δ -phase reflections were detected.

Another key observation is the evolution of α -phase peak intensity, which reaches a maximum at a deposition time of 200 minutes. Beyond this point, the intensity of the two most prominent peaks begins to decline. The initial increase in peak intensity suggests coherent growth of the polycrystalline film, whereas the subsequent decrease likely indicates the onset of disorder in the upper layers (Figure S8). As deposition progresses, the substrate peak intensity gradually decreases, reflecting reduced X-ray penetration due to increasing perovskite thickness. Simultaneously, the (200) and (210) peak intensities increase, confirming the formation of a thicker and more crystalline perovskite layer. However, at 300 minutes of deposition (Type-300), this trend reverses, suggesting the formation of an amorphous overlayer or increased structural disorder that diminishes the crystalline signal, potentially due to diffuse scattering effects.

To address the issue observed in the Type-300 samples, an intermediate annealing step is introduced in samples named Type-300A to stabilize the perovskite structure and promote further growth of the absorber layer, with the aim of enhancing overall device performance. Structurally, as shown in Figure 3, the Type-300A samples exhibit higher α -phase peak intensities compared to the Type-300, indicating that the additional top-layer deposition is crystalline rather than amorphous and that integrates with the underlying structure, supporting coherent vertical growth.

A synoptics view of the impact of substrates on the phase purity is shown in Figure 4. Here, we plot the phase composition of the analyzed samples as estimated by summing the intensities of the diffraction peaks corresponding to each phase normalized to the total intensity of each spectrum. The data show that the intensity associated with the α -phase increases progressively from PTAA to SAM, and also increasing the

substrate temperature from 20 °C to 60 °C. In contrast, the δ -phase exhibits the opposite trend: as the perovskite deposition time increases, the percentage of the δ -phase progressively decreases, except for the Type-300. Notably, SAM samples consistently show a lower fraction of δ -phase compared to PTAA, even at short deposition times. Interestingly, in samples deposited on SAM at 60 °C, the δ -phase component is completely absent, suggesting that higher substrate temperatures promote the stabilization of a pure α -phase on SAM. Moreover, it is important to note that the α -phase content is increased in the Type-300A samples compared to the Type-300, wherever a direct comparison is possible. This supports the conclusion that the intermediate annealing step facilitates crystalline structure recovery in the subsequent layer.

Structural coherence was investigated by observing the relation between q and $v(h^2 + k^2 + l^2)$ for the reflections attributed to the α -phase in PTAA and SAM samples (Figure S10). The linear relation confirms the expected crystallographic relationship and allows for an exact determination of the lattice parameters.

The calculated lattice parameters for both the cubic (α -phase) and hexagonal (δ -phase) structures are presented in Figure 5. For the α -phase, no significant differences are observed between PTAA and SAM samples, as the cubic lattice parameter remains essentially constant at an average value of 6.34 ± 0.01 Å across all cases. A slight decrease to 6.33 ± 0.01 Å is found for the PTAA_60 samples, which can be mainly attributed to the smaller number of available data points. Both values, however, are lower than the reported theoretical lattice parameter for α -FAPbI₃, 6.36 Å⁴⁶, indicating the presence of compressive strain with a magnitude of approximately 0.3–0.5%.

Kim *et al.* highlighted that the α -FAPbI₃ phase possesses a mechanically soft lattice, rendering it highly sensitive to strain; and even small distortions can significantly affect its structural stability and phase transitions.⁴⁷ In

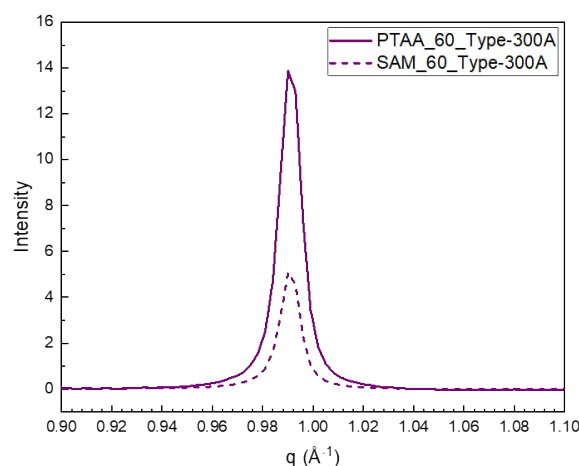


Figure 6: Comparison of the absolute intensity of the (100) α -phase peak of FAPbI₃ perovskite for Type-300A films deposited at 60 °C on PTAA (solid line) and SAM (dashed line).



1 polycrystalline perovskite films, residual strain in
2 perovskite films primarily arises from experimental

3 conditions, including the material composition, the choice
4 of underlayer for film growth, and thermal stress induced

View Article Online
DOI: 10.1039/D5TA0193E

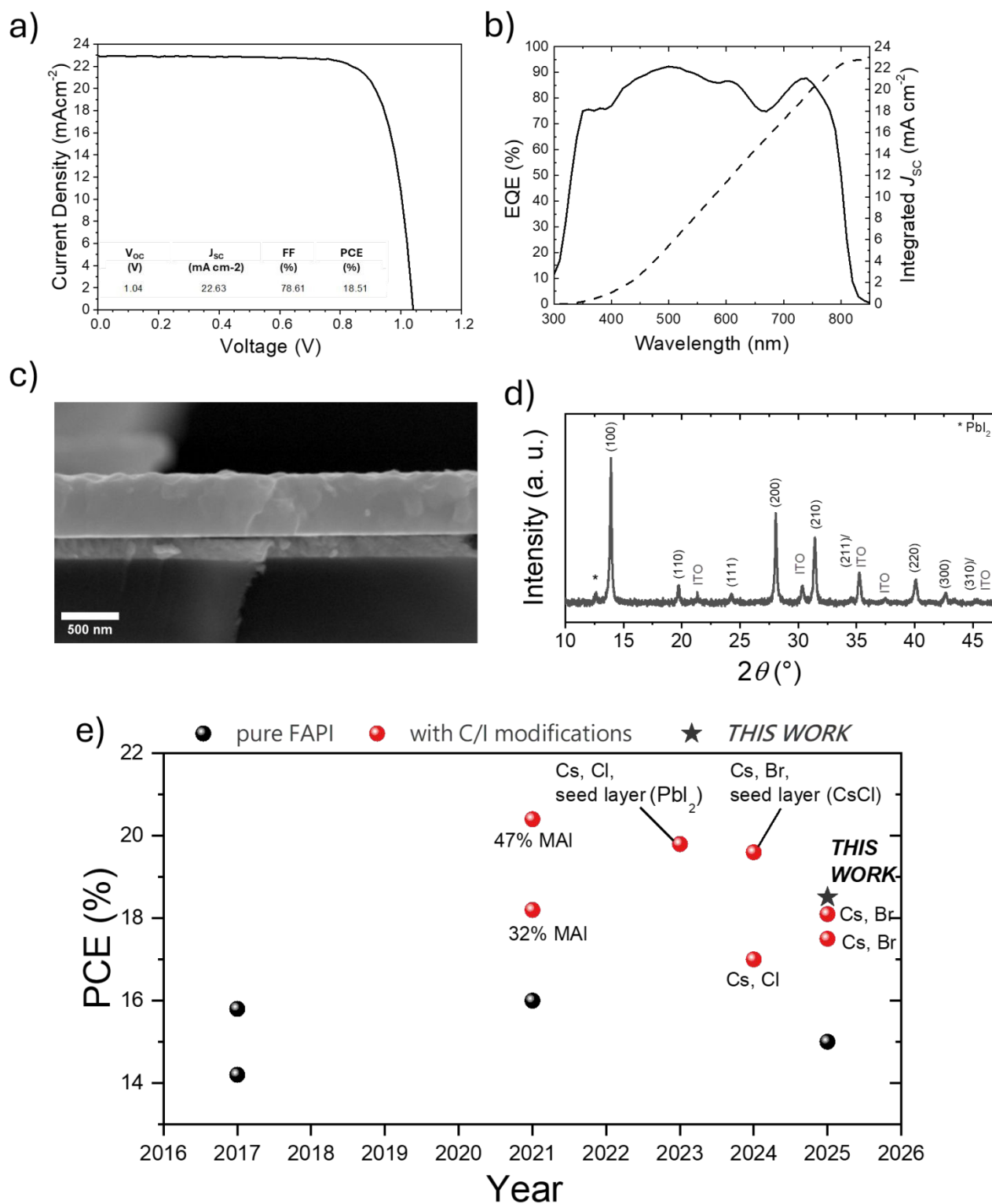


Figure 7: a) J - V and b) EQE of Type-300A FAPI-based p - i - n device. The relative electrical parameters are also reported in a). Statistical distribution of the electrical parameters of the same batch is reported in the SI. c) SEM cross-section and d) XRD pattern of glass/ITO/Type-300A FAPI. e) Power conversion efficiency (PCE) evolution of co-evaporated FAPbI₃ solar cells over time. Devices based on pure FAPbI₃ (black) and devices with FAPI based on compositional or interfacial (C/I) modifications (red) are compared. The type of C/I modification used is indicated next to each red data point.^{38,39,41,66–69} The details are shown in Table S2.



1 during annealing process or subsequent measurements.
2^{48,49} Importantly, moderate compressive strain has been
3 shown to be beneficial, as it suppresses octahedral tilting,
4 thereby preserving the α -phase structure, limiting ion
5 migration, and elevating the α - to δ -phase transition
6 barrier.^{47,50,51}

7 Several recent studies further suggest that perovskite
8 devices achieve higher efficiencies under compressive
9 strain, which improves band alignment for more effective
10 charge extraction and increases carrier mobility, while
11 simultaneously increasing the formation energy of halide
12 vacancies and suppressing nonradiative recombination.
13 Together, these effects boost open-circuit voltage and fill
14 factor, ultimately contributing to enhanced device
15 performance.^{52–55}

16 Regarding the δ -phase lattice parameters, a more detailed
17 analysis has been performed (Figure S11), relating the unit
18 cell volume of the δ -phase with the deposition time for
19 SAM and PTAA samples where this phase is detected.
20 Overall, the mean unit cell volume of the δ -phase remains
21 approximately 519 Å³, indicating a consistent structure
22 across samples.

23 However, diffraction data indicate that, although the
24 perovskite absorber deposited on the SAM exhibits
25 improved crystallinity compared to PTAA, the XRD peak
26 intensity is lower (see Figure 6). The reduced intensity may
27 be attributed to a smaller effective volume of the
28 deposited absorber, which arises from differences in
29 nucleation dynamics on the two studied HTLs. This
30 suggests that the same deposition process may be less
31 effective for one HTL compared to the other. Furthermore,
32 the perovskite film grown on SAM exhibits a higher density
33 of smaller grains compared to the PTAA-based samples
34 (Figure S12).

35 These structural effects are closely related to the
36 interfacial properties of the SAM itself. The molecular
37 packing and orientation of MeO-2PACz, for example, play
38 a critical role in directing the crystallization of the
39 perovskite layer. In particular, despite this favorable
40 influence on crystallinity, such a disordered or excessive
41 SAM can be detrimental to device performance. It may
42 introduce interfacial barriers that hinder efficient charge
43 extraction or lead to variability across large areas. A major
44 limitation is the lack of processing reproducibility,
45 especially over large areas, where achieving uniform SAM
46 coverage is difficult. This directly affects the homogeneity
47 of the device performance.^{56–58} Additionally, issues such as
48 micelle formation during deposition can lead to non-
49 uniform film morphology, which in turn hinders efficient
50 interfacial charge transfer.^{59,60}

51 To verify the impact of HTL and deposition conditions on
52 solar cells obtained with co-evaporated FAPI, we realized
53 PSCs in $p-i-n$ configuration with the following stack:
54 glass/ITO/HTL/FAPI/PCBM/BCP/Cu. Further details are
55 reported in the Experimental section. SAM-based devices
56 exhibit a larger spread of photovoltaic parameters
57 compared to PTAA (Figure S13), with an overall reduction

58 in PCE mainly driven by a substantial drop in J_{sc} . This drop
59 is likely associated with an excess of organic cations
60 incorporated into the perovskite film, which may arise
61 from altered surface chemistry and growth dynamics, as
62 reported earlier.³⁹

63 We also performed analogous tests on washed SAM
64 substrates, as reported in SI, observing a similar reduction
65 in J_{sc} , but with improved reproducibility. In this case, the
66 behavior may instead be associated with a relative
67 deficiency of FAI during growth.

68 In light of these structural and performance-related
69 challenges, PTAA was selected as the HTL for the
70 subsequent device fabrication to ensure improved
71 reproducibility and interface control.

72 This choice does not imply an intrinsic superiority of PTAA
73 over MeO-2PACz, but rather reflects the better
74 compatibility of the current deposition protocol with
75 PTAA. Additional engineering of the MeO-
76 2PACz/perovskite interface may offer further performance
77 gains, but this aspect is beyond the scope of the present
78 work.

79 We initially explored FAPbI₃ deposition through a
80 continuous 200-minute evaporation process, during which
81 no changes or replacements of the FAI source were made.
82 The resulting devices exhibited good fill factors (FFs), but
83 limited V_{oc} and very low J_{sc} , due to reduced EQE (Figure
84 S16-A,B). These performance losses are attributed to high
85 recombination, consistent with the poor film quality. To
86 mitigate interfacial recombination at surface and grain
87 boundary defects, phenylethylammonium chloride (PEACl)
88 was deposited by thermal evaporation on top of
89 perovskite as a surface passivation layer. Although vapour-
90 phase treatments based on PEA⁺ cations have been
91 previously explored^{61,62}, the use of evaporated PEACl as a
92 passivation layer has not yet been reported, to the best of
93 our knowledge. The introduction of PEACl led to an
94 improvement in V_{oc} (up to ~1.1 V, see Figure S16-17),
95 confirming effective passivation. However, short-circuit
96 current densities were still limited due to the persistent
97 poor quality of the FAPI film.

98 By combining PEACl passivation with the modified FAPI
99 deposition protocol where two FAI sources were
100 employed sequentially, each for 100 min (Type-200), we
101 achieved a substantial enhancement in photocurrent and
102 EQE, with J_{sc} values approaching 21 mA cm⁻² (Figure S16-
103 C,D, Figure S17). This optimization led to the best device
104 efficiency of 17.55% (Figure S16-C).

105 Building on the structural analysis previously presented,
106 Type 300-A deposition was selected among Type-300 and
107 Type-300A evaporation protocols with the aim of
108 increasing the FAPI absorber thickness while mitigating the
109 degradation of FAI during prolonged thermal evaporation.
110 In fact, as previously shown, the Type-300A method
111 resulted in films with superior crystallinity compared to
112 Type-300, leading to a more coherent perovskite layer. The
113 perovskite thickness was increased from 280 nm (Type-
114 200) up to 400 nm (Type-300A), without compromising the



1 morphology and the phase (Figure S18-c, d, Figure 7-c, d).
2 The (100) plane of the α -phase is located at 13.91°, slightly
3 shifting from the previous of Type-200, which is at 13.94°.
4 This is attributed to strain relaxation with increased
5 thickness.^{63,64}

6 Type-300A-based devices showed an enhanced EQE, with
7 integrated J_{sc} approaching 23 mA cm⁻² achieving a
8 maximum PCE of 18.5% (Figure 7-a, b; statistics in Figure
9 S19). Notably, this represents one of the highest
10 efficiencies reported for co-evaporated FAPbI₃ films
11 without any compositional modification (either cationic or
12 anionic), or seed-layer-assisted interfacial engineering,
13 highlighting the intrinsic quality of the co-evaporated
14 FAPbI₃ films (Figure 7-e).

15 The long-term stability of the devices was evaluated
16 through shelf-life measurements and ISOS-L1 operational
17 stability tests (Figure S18). Under shelf-life conditions, the
18 unencapsulated Type-300A-based devices stored in an N₂-
19 filled glovebox exhibit negligible degradation, maintaining
20 a stable PCE for 1000 hours (Figure S20-a).

21 Operational stability under continuous illumination (ISOS-
22 L1), shown in Figure S20-b, reveals an improved durability
23 for the optimized Type-300A architecture, reaching a T_{80}
24 lifetime (defined as the time at which the PCE drops to 80%
25 of its initial value) of 400 hours. In contrast, devices based
26 on the Continuous-200 configuration show a significantly
27 faster performance decay, indicating reduced intrinsic
28 operational stability.

29 3. Conclusions

30 In this work, we demonstrate a fully additive-free thermal
31 co-evaporation process for pure FAPbI₃ perovskite films,
32 achieving high phase purity and crystallinity through
33 control of deposition dynamics and substrate engineering.

34 By employing multiple FAI sources in a sequential
35 evaporation scheme, we mitigate thermal alterations of
36 the organic precursor and enable the deposition of thick,
37 uniform perovskite layers. Furthermore, the introduction
38 of an intermediate annealing step proves to be critical for
39 enhancing crystallization quality, especially in thicker films,
40 promoting grain growth and improved structural
41 coherence.

42 We also provide an investigation of the effect of substrate
43 temperature on perovskite film formation. Among the
44 conditions tested, deposition at 60 °C yields the best
45 structural quality, as evidenced by enhanced α -phase
46 formation and suppression of undesired hexagonal
47 phases. Complementary morphological and structural
48 characterizations, including XRD and GIXD, confirm the
49 improved ordering and orientation of the perovskite films
50 at this temperature. By leveraging a multi-source
51 evaporation scheme, an intermediate annealing step, and
52 optimized substrate temperatures, we establish a
53 framework for improving crystallization dynamics and
54 phase development.

55 Moreover, the role of the hole transport layer is shown to
56 be pivotal in determining both film quality and device
57 reproducibility, under the same growth protocol. While
58 MeO-2PACz enhances α -phase formation, it suffers from
59 limited processing uniformity and detrimental
60 morphological effects. PTAA, by contrast, enables more
61 reproducible growth and uniform film morphology,
62 ultimately resulting in higher device performance. Using
63 PTAA as the HTL, we achieve a power conversion efficiency
64 of 18.5% in a $p-i-n$ device configuration with pure,
65 thermally evaporated FAPbI₃. The devices demonstrated
66 excellent long-term stability (shelf-life), as well as stable
67 operation under continuous illumination, reaching a T_{80}
68 lifetime of 400 h under ISOS-L1 conditions when
69 encapsulated.

70 This work offers key insights into the interdependence of
71 process conditions (including precursor evaporation,
72 substrate conditions, and interfacial layers), providing a
73 pathway toward more reliable and scalable fabrication of
74 high-performance vapor-deposited perovskite solar cells.

75 4. Experimental

76 4.1 Materials

77 Indium–tin oxide (ITO)-coated glasses ($R_{SH} = 7 \Omega \text{ sq}^{-1}$) were
78 purchased from Kintec. Formamidinium iodide (FAI) and
79 phenethylammonium chloride (PEACl) were purchased
80 from GreatCell Solar. Lead(II)iodide (PbI₂) and MeO-2PACz
81 ((2-(3,6-Dimethoxy-9H-carbazol-9-yl)ethyl)phosphonic
82 acid) were purchased from TCI. Poly[bis(4-phenyl)(2,4,6-
83 trimethylphenyl)amine] (PTAA) SOL2426L (low molecular
84 weight, 5 – 10 kDa) was purchased from Solaris Chem.
85 Bathocuproine (BCP) and copper beads (Cu beads),
86 ethanol (EtOH)(anhydrous, $\geq 99.8\%$), acetone ($\geq 99.5\%$),
87 chlorobenzene (CB) (99.8%), 1,2-dichlorobenzene (DCB)
88 (99%), toluene ($>99.7\%$), and 2-propanol (IPA) (anhydrous,
89 99.5%) were purchased from Sigma-Aldrich.
90 Buckminsterfullerene C60 (C60 purity 99.5%) and [6,6]-
91 phenyl-C60-butyric acid methyl ester (C60-PCBM purity
92 99%) were purchased from Special Carbon Products. Silver
93 (Ag) paste 7713 was purchased from Dupont.

95 4.2 Device fabrication

96 The perovskite solar cells were fabricated using an
97 inverted ($p-i-n$) planar architecture. Glass/ITO substrates
98 were initially patterned using a Yb:KGW raster-scanning
99 laser (Wophotonics, $\lambda = 355 \text{ nm}$) and subsequently cut into
100 $2.5 \times 2.5 \text{ cm}^2$ samples. The patterned substrates were
101 cleaned sequentially in an ultrasonic bath: first in a 2%
102 Hellmanex detergent solution in deionized water, followed
103 by acetone, and finally isopropanol, each for 15 minutes.
104 Any residual solvents were removed using a stream of air.
105 The substrates were then treated with UV-ozone for 15
106 minutes using a PSD Pro Series Digital UV Ozone System
107 (Novascan) to eliminate remaining organic contaminants.



1 For PTAA deposition, the substrates were transferred to an
2 air-filled flowbox, where a solution of PTAA (2 mg/mL in
3 toluene) was spin-coated at 5000 rpm for 20 seconds. In
4 contrast, for SAM deposition, the substrates were
5 transferred to a nitrogen-filled glovebox and coated with
6 MeO-2PACz (0.33 mg/mL in anhydrous ethanol) via spin-
7 coating at 4000 rpm for 30 seconds. All coated samples
8 were subsequently annealed at 100 °C for 10 minutes.

9 After cooling, the substrates were loaded into a Kenosistec
10 KE 500 K thermal evaporator for the co-deposition of the
11 FAPbI₃ perovskite layer. The inner shielding temperature
12 was set to -25 °C, and the substrate temperature was
13 maintained at either 20 °C or 60 °C, with a substrate holder
14 rotation speed of 15 rpm. The amount of precursor loaded
15 into each crucible was measured prior to each deposition
16 process. Specifically, 2.2 g of PbI₂ and 3.0 g of FAI were
17 loaded into their respective crucibles. The crucibles used
18 in our system are conical, with a volume of 10 cm³. Co-
19 deposition began once the crucible temperatures reached
20 their target temperatures: 345 °C for PbI₂ and 210 °C for
21 FAI, according to the procedures shown in the manuscript
22 (Figure 1) and as shown in Figure S23-a. In case of fresh FAI
23 material, a degassing procedure (preconditioning), during
24 which a pressure increase in the chamber was observed
25 (Figure S23-b), was performed prior to deposition.³² For
26 Type-200 samples, two different FAI sources were
27 employed sequentially, each for 100 min. After opening
28 the chamber, annealing the samples, and reloading the FAI
29 material, an additional 100 min deposition was carried out
30 to obtain Type-300A FAPI films. The preconditioning step
31 was performed prior to each deposition involving freshly
32 loaded FAI material. The chamber pressure during
33 deposition was $4-5 \times 10^{-6}$ mbar. After the process, the
34 samples were annealed in a nitrogen atmosphere at 150 °C
35 for 15 minutes.

36 To passivate the perovskite layer, PEACl was thermally
37 evaporated at 180 °C for 15 minutes, with no additional
38 annealing.

39 For the electron transport layer (ETL), PCBM/BCP stack was
40 deposited by spin-coating PCBM (27 mg/mL in a 0.75:0.25
41 CB:DCB mixture) was stirred overnight, then spin-coated at
42 1350 rpm for 20 seconds and annealed at 100 °C for 3
43 minutes. Spin-coating of BCP solution (0.5 mg/mL in IPA)
44 was performed at 2300 rpm for 15 seconds, without
45 further drying.

46 Finally, 100 nm of copper (Cu) was deposited by thermal
47 evaporation using a shadow mask to define four individual
48 cells per substrate.

49 The ISOS-L-1 tests were performed with an Arkeo-
50 multichannel (Cicci Research company) based on 32 fully

51 independent Source Meter Unit (± 10 V @ ± 250 mA) and
52 an ARKEO Light soaker (VIS version) with low mismatch
53 LED based system (400–750 nm). A standard
54 Perturb&Observe tracking algorithm was selected with
55 a *J*-*V* scan every 3 hours. The measurements were done in
56 ambient conditions without temperature control, and the
57 cells were encapsulated prior to the test.⁶⁵

58 4.3 Characterization

59 *J*-*V* measurements of the perovskite solar cells (PSCs) were
60 carried out using a Class-A solar simulator (ABET 2000)
61 equipped with an AM1.5G filter (ABET). The simulator was
62 calibrated to 1 sun illumination using a silicon reference
63 cell (RR-226-O, RERA Solutions). *J*-*V* characterization
64 under both forward and reverse scan directions was
65 performed using the Arkeo platform (Cicci Research s.r.l.),
66 with a voltage step of 20 mV and a scan rate of 200 mV/s.
67 An opaque mask defining an active area of 0.09 cm² per
68 pixel was applied during the measurements to ensure
69 accurate illumination and measurement. External
70 quantum efficiency (EQE) measurements were conducted
71 using the Arkeo system, which features a 150 W xenon
72 lamp and a double monochromator covering the 300–
73 1400 nm range. A silicon photodiode was used for incident
74 light calibration before EQE measurement.

75 X-ray diffraction (XRD) measurements were carried out
76 using a Rigaku SmartLab diffractometer operating in (θ -
77 2θ) Bragg-Brentano geometry. The system was equipped
78 with a Cu K α radiation source ($K\alpha_1 = 1.54056$ Å, $K\alpha_2 =$
79 1.54439 Å) and a D/teX Ultra 250 silicon strip detector. XRD
80 patterns were recorded in a single scan over the 2θ range
81 of 5° to 50°, with a step size of 0.02°, a scan rate of 8°/min,
82 and a 5 mm entrance slit.

83 Scanning Electron Microscopy (SEM) measurements were
84 performed by using a FESEM, Tescan Mira 3 LMU FEG. The
85 thickness measurements were acquired with a Dektak
86 Veeco profilometer.

87 ¹H-NMR spectra were recorded on a Bruker AVANCE 600
88 NMR spectrometer (Rheinstetten, Germany) operating at
89 a proton frequency of 600.13 MHz in DMSO-d₆. Chemical
90 shifts (δ) are given in ppm relative to tetramethylsilane
91 (TMS).

92 Grazing Incidence X-ray Diffraction (GIXD) measurements
93 were performed at the Surfaces Interfaces X-ray Scattering
94 (SixS) beamline at the SOLEIL synchrotron facility (Paris,
95 France). Samples were introduced into an ultra-high
96 vacuum (UHV) chamber and analyzed using an integrated
97 six-circle diffractometer equipped with a 2D hybrid pixel
98 detector (XPAD S70). A 2D hybrid pixel detector (XPAD S70)
99 was used to collect the diffracted intensity, and the
100 BINoculars program was used to process the whole data



1 set Monochromatic X-rays with a photon energy of 18 keV
 2 were used for structural characterization. Preliminary X-
 3 ray reflectivity (XRR) measurements were performed to
 4 determine the optimal incidence angle. The chosen angle
 5 was set to 0.135° above the critical angle of the film and
 6 below that of the substrate, ensuring full penetration of
 7 the X-ray beam throughout the entire film thickness.
 8 Under these conditions, the collected signal originates
 9 from the whole bulk of the film while minimizing any
 10 contribution from the substrate. The diffracted intensity
 11 collected by the detector were processed through
 12 BINoculars program and GIXD scans were acquired at fixed
 13 angle over a scattering vector (q) range of 0.76 Å⁻¹ to 5 Å⁻¹,
 14 with a step size of 0.003 Å⁻¹.

15 Author contributions

16 **F.Z., E.M.:** Conceptualization, Writing – original draft, Software,
 17 Investigation, Formal analysis, Data curation, Investigation,
 18 Writing – review & editing. **S.P., F.T., E.G, V.R., M.D.G., F.D.G.:**
 19 Formal analysis, Investigation. **A.C.:** Data curation. **R.F.:** Formal
 20 analysis, Data curation, Writing – review & editing. **A.D.C.:**
 21 Conceptualization, Writing – review & editing, Supervision,
 22 Project administration, Funding acquisition.

23 Conflicts of interest

24 There are no conflicts to declare.

25 Data availability

26 Data for this article, including XRD, J-V, EQE, state-of-the-
 27 art references on co-evaporated FAPI, are available at
 28 ZENODO at <https://doi.org/10.5281/zenodo.17649740>.

29 Acknowledgements

30 E.M. acknowledges the LUMINOSITY project funded by the
 31 European Union's Horizon Europe Research and
 32 Innovation Programme under grant agreement no.
 33 101147653. F.Z. acknowledges the support of MASE
 34 (Ministero dell'Ambiente e della Sicurezza Energetica) in
 35 the framework of the Operating Agreement with ENEA for
 36 Research on the Electric System 2025-2027. A.D.C.
 37 acknowledges TANDEM project of Ministero della
 38 Transizione Ecologica (Italy), funded on 20/09/2021 (CUP:
 39 B83C21001790005). The authors acknowledge Dr. Lucia V.
 40 Mercardo for fruitful discussion. The authors wish to thank
 41 the SixS beamline staff for the scientific and technical
 42 support provided during the experiment at the SOLEIL
 43 synchrotron facility.

44 Notes and references

45 1 A. U. I. Shah and E. L. Meyer, *Sol. Energy*, 2025, **286**,
 46 113172.

- 47 2 W. Xiang and W. Tress, *Adv. Mater.*,
 48 DOI:10.1002/adma.201902851. DOI: 10.1039/D5EL00193E
 49 3 W. Shockley and H. J. Queisser, *J. Appl. Phys.*, 1961, **32**,
 50 510–519.
 51 4 Q. Lin, D. J. Kubicki, M. Omrani, F. Alam and M. Abdi-Jalebi,
 52 *J. Mater. Chem. C*, 2023, **11**, 2449–2468.
 53 5 H.-S. Kim, A. Hagfeldt and N.-G. Park, *Chem. Commun.*,
 54 2019, **55**, 1192–1200.
 55 6 Y. Ahmed, X. Qi, P. Moazzezi and M. I. Saidaminov, *ACS*
 56 *Energy Lett.*, DOI:10.1021/acscenergylett.5c03275.
 57 7 A. J. Knight and L. M. Herz, *Energy Environ. Sci.*, 2020, **13**,
 58 2024–2046.
 59 8 L. Tian, J. Xue and R. Wang, *Electronics*, 2022, **11**, 700.
 60 9 S. Lee, D. Lee, S. Choi, S. Jung, J. Lee, M. Kim, J. Park and J.
 61 Lee, *Sol. RRL*, DOI:10.1002/solr.202300958.
 62 10 J. Zhou, Y. Gao, Y. Pan, F. Ren, R. Chen, X. Meng, D. Sun, J.
 63 He, Z. Liu and W. Chen, *Sol. RRL*,
 64 DOI:10.1002/solr.202200772.
 65 11 Y. Liang, F. Li, X. Cui, T. Lv, C. Stampfl, S. P. Ringer, X. Yang,
 66 J. Huang and R. Zheng, *Nat. Commun.*, 2024, **15**, 1707.
 67 12 J. Hidalgo, W. Kaiser, Y. An, R. Li, Z. Oh, A.-F. Castro-
 68 Méndez, D. K. LaFollette, S. Kim, B. Lai, J. Breternitz, S.
 69 Schorr, C. A. R. Perini, E. Mosconi, F. De Angelis and J.-P.
 70 Correa-Baena, *J. Am. Chem. Soc.*,
 71 DOI:10.1021/jacs.3c05657.
 72 13 B. Charles, J. Dillon, O. J. Weber, M. S. Islam and M. T.
 73 Weller, *J. Mater. Chem. A*, 2017, **5**, 22495–22499.
 74 14 Z. Zhou, S. Pang, F. Ji, B. Zhang and G. Cui, *Chem. Commun.*,
 75 2016, **52**, 3828–3831.
 76 15 G. E. Eperon, C. E. Beck and H. J. Snaith, *Mater. Horizons*,
 77 2016, **3**, 63–71.
 78 16 J. Hieulle, X. Wang, C. Stecker, D.-Y. Son, L. Qiu, R.
 79 Ohmann, L. K. Ono, A. Mugarza, Y. Yan and Y. Qi, *J. Am.*
 80 *Chem. Soc.*, 2019, **141**, 3515–3523.
 81 17 A. Touré, A. Bouich, B. M. Soucasse and D. Soro, *Opt.*
 82 *Mater. (Amst.)*, 2023, **135**, 113334.
 83 18 H. B. Lee, R. Sahani, V. Devaraj, N. Kumar, B. Tyagi, J. Oh
 84 and J. Kang, *Adv. Mater. Interfaces*,
 85 DOI:10.1002/admi.202201658.
 86 19 W. Cheng, X. He, J. Wang, W. Tian and L. Li, *Adv. Mater.*,
 87 DOI:10.1002/adma.202208325.
 88 20 Y. Zhang, T. Yang, S.-U. Lee, S. Liu, K. Zhao and N.-G. Park,
 89 *ACS Energy Lett.*, 2024, **9**, 159–167.
 90 21 A. Krishna, V. Škorjanc, M. Dankl, J. Hieulle, H. Phirke, A.
 91 Singh, E. A. Alharbi, H. Zhang, F. Eickemeyer, S. M.
 92 Zakeeruddin, G. N. M. Reddy, A. Redinger, U. Rothlisberger,
 93 M. Grätzel and A. Hagfeldt, *ACS Energy Lett.*, 2023, **8**,
 94 3604–3613.
 95 22 Y. Wang, C. Yang, Z. Wang, G. Li, Z. Yang, X. Wen, X. Hu, Y.
 96 Jiang, S. Feng, Y. Chen, G. Zhou, J. Liu and J. Gao, *Small*,
 97 DOI:10.1002/smll.202306954.
 98 23 Z. Huang, Y. Bai, X. Huang, J. Li, Y. Wu, Y. Chen, K. Li, X. Niu,
 99 N. Li, G. Liu, Y. Zhang, H. Zai, Q. Chen, T. Lei, L. Wang and H.
 100 Zhou, *Nature*, 2023, **623**, 531–537.
 101 24 H. Cao, T. Li, L. Zhao, Y. Qiang, X. Zheng, S. Dai, Y. Chen, Y.
 102 Zhu, L. Zhao, R. Cai, Z. Sun, F. Li, Y. Yang, L. Zhang, H.-L. Yip
 103 and Z. Yu, *ACS Energy Lett.*, 2025, **10**, 2017–2025.



- 1 25 T. Abzieher, D. T. Moore, M. Roß, S. Albrecht, J. Silvia, H. 58 44 M. V. Khenkin, E. A. Katz, A. Abate, G. Bardizza, J. J. Berry, DOI:10.1039/D5EE00193E
 2 Tan, Q. Jeangros, C. Ballif, M. T. Hoerantner, B.-S. Kim, H. 59 C. Brabec, F. Brunetti, V. Bulović, Q. Burlingame, A. D
 3 Bolink, P. Pistor, J. C. Goldschmidt, Y.-H. Chiang, S. D. 60 Carlo, R. Cheacharoen, Y. B. Cheng, A. Colsmann, S. Cros, K.
 4 Stranks, J. Borchert, M. D. McGehee, M. Morales-Masis, J. 61 Domanski, M. Dusza, C. J. Fell, S. R. Forrest, Y. Galagan, D.
 5 B. Patel, A. Bruno and U. W. Paetzold, *Energy Environ. Sci.* 62 Di Girolamo, M. Grätzel, A. Hagfeldt, E. von Hauff, H.
 6 2024, **17**, 1645–1663. 63 Hoppe, J. Kettle, H. Köbler, M. S. Leite, S. (Frank) Liu, Y. L.
 7 26 J. Luo, J. Li, L. Grater, R. Guo, A. R. bin Mohd Yusoff, E. 64 Loo, J. M. Luther, C. Q. Ma, M. Madsen, M. Manceau, M.
 8 Sargent and J. Tang, *Nat. Rev. Mater.*, 2024, **9**, 282–294. 65 Matheron, M. McGehee, R. Meitzner, M. K. Nazeeruddin,
 9 27 J. Li, H. A. Dewi, H. Wang, J. Zhao, N. Tiwari, N. Yantara, T. 66 A. F. Nogueira, Ç. Odabaşı, A. Osherov, N. G. Park, M. O.
 10 Malinauskas, V. Getautis, T. J. Savenije, N. Mathews, S. 67 Reese, F. De Rossi, M. Saliba, U. S. Schubert, H. J. Snaith, S.
 11 Mhaisalkar and A. Bruno, *Adv. Funct. Mater.*, 2021, 68 D. Stranks, W. Tress, P. A. Troshin, V. Turkovic, S. Veenstra,
 12 **2103252**, 1–11. 69 I. Visoly-Fisher, A. Walsh, T. Watson, H. Xie, R. Yildirim, S.
 13 28 F. U. Kosasih, E. Erdenebileg, N. Mathews, S. G. Mhaisalkar 70 M. Zakeeruddin, K. Zhu and M. Lira-Cantu, *Nat. Energy*,
 14 and A. Bruno, *Joule*, 2022, **6**, 2692–2734. 71 2020, **5**, 35–49.
 15 29 M. Roß, M. B. Stutz and S. Albrecht, *Sol. RRL*, 72 45 S. Kralj and M. Morales-Masis, *Matter*, 2024, **7**, 3238–3240.
 16 DOI:10.1002/solr.202200500. 73 46 M. T. Weller, O. J. Weber, J. M. Frost and A. Walsh, *J. Phys.*
 17 30 B.-S. Kim, M.-H. Choi, M.-S. Choi and J.-J. Kim, *J. Mater.* 74 46 *Chem. Lett.*, 2015, **6**, 3209–3212.
 18 *Chem. A*, 2016, **4**, 5663–5668. 75 47 H. S. Kim and N. G. Park, *Adv. Energy Mater.*, 2025, **15**, 1–
 19 31 M. J. Bækbo, O. Hansen, I. Chorkendorff and P. C. K. 76 47 10.
 20 Vesborg, *RSC Adv.*, 2018, **8**, 29899–29908. 77 48 H.-S. Kim and N.-G. Park, *NPG Asia Mater.*, 2020, **12**, 78.
 21 32 M. Kroll, S. D. Öz, R. Ji, Z. Zhang, T. Schramm, T. Antrack, 78 49 H. Zhang and N. G. Park, *Angew. Chemie - Int. Ed.*,
 22 Olthof, Y. Vaynzof and K. Leo, *Sustain. Energy Fuels*, 79 49 DOI:10.1002/anie.202212268.
 23 DOI:10.1039/d2se00373b. 80 50 Y. Chen, Y. Lei, Y. Li, Y. Yu, J. Cai, M. H. Chiu, R. Rao, Y. Gu,
 24 33 J. Petry, V. Škorjanc, A. Diercks, T. Feeney, A. Morsa, S. R. 81 50 C. Wang, W. Choi, H. Hu, C. Wang, Y. Li, J. Song, J. Zhang, B.
 25 Kimmig, J. Baumann, F. Löffler, S. Auschill, J. Damm, D. 82 Qi, M. Lin, Z. Zhang, A. E. Islam, B. Maruyama, S. Dayeh, L.
 26 Baumann, F. Laufer, J. Kurpiers, M. Müller, L. Korte, S. 83 J. Li, K. Yang, Y. H. Lo and S. Xu, *Nature*, 2020, **577**, 209–
 27 Albrecht, M. Roß, U. W. Paetzold and P. Fassl, *EES Sol.*, 84 215.
 28 2025, **1**, 404–418. 85 51 J. Dai, T. Li, X. Li, C. Xu, M. Zhao, H. Cai and X. Wu, *Phys.*
 29 34 M. Roß, L. Gil-Escrig, A. Al-Ashouri, P. Tockhorn, M. Jošt, 86 51 *Chem. Chem. Phys.*, 2025, **27**, 16783–16793.
 30 Rech and S. Albrecht, *ACS Appl. Mater. Interfaces*, 2020, 87 52 Y. Zhou, Z. Guo, S. M. H. Qaid, Z. Xu, Y. Zhou and Z. Zang,
 31 **12**, 39261–39272. 88 52 *Sol. RRL*, 2023, **7**, 1–26.
 32 35 R. Kottokkaran, H. A. Gaonkar, H. A. Abbas, M. Noack and 89 53 G. Liu, M. Ghasemi, Q. Wei, G. Zhang, J. Luo, D. Su, B. Jia, Y.
 33 V. Dalal, *J. Mater. Sci. Mater. Electron.*, 2019, **0**, 0. 90 Yang and X. Wen, *ACS Appl. Mater. Interfaces*, 2025, **17**,
 34 36 K. B. Lohmann, J. B. Patel, M. U. Rothmann, C. Q. Xia, R. D. 91 53 36706–36716.
 35 J. Oliver, L. M. Herz, H. J. Snaith and M. B. Johnston, 92 54 B. Jin, J. Cao, R. Yuan, B. Cai, C. Wu and X. Zheng, *Adv.*
 36 DOI:10.1021/acseenergylett.0c00183. 93 54 *Energy Sustain. Res.*, DOI:10.1002/aesr.202200143.
 37 37 C. Chen, H. Kang, S. Hsiao, P. Yang, K. Chiang and H. Lin, 94 55 X. Jiang, X. Wang, X. Wu, S. Zhang, B. Liu, D. Zhang, B. Li, P.
 38 *Adv. Mater.*, 2014, **26**, 6647–6652. 95 55 Xiao, F. Xu, H. Lu, T. Chen, A. K. Y. Jen, S. Yang and Z. Zhu,
 39 38 L. Gil-Escrig, J. Nespoli, F. D. Elhorst, F. Ventosinos, C. 96 55 *Adv. Energy Mater.*, 2023, **13**, 1–8.
 40 Roldán-Carmona, L. J. A. Koster, T. J. Savenije, M. Sessolo 97 56 T. Liu, C. Luo, R. He, Z. Zhang, X. Lin, Y. Chen and T. Wu,
 41 and H. J. Bolink, *EES Sol.*, 2025, **1**, 391–403. 98 56 *Adv. Mater.*, DOI:10.1002/adma.202502032.
 42 39 T. Feeney, J. Petry, A. Torche, D. Hauschild, B. Hacene, C. 99 57 C. Fei, A. Kuvayskaya, X. Shi, M. Wang, Z. Shi, H. Jiao, T. J.
 43 Wansorra, A. Diercks, M. Ernst, L. Weinhardt, C. Heske, 100 Silverman, M. Owen-Bellini, Y. Dong, Y. Xian, R. Scheidt, X.
 44 Gryn'ova, U. W. Paetzold and P. Fassl, *Matter*, 2024, **7**, 101 Wang, G. Yang, H. Gu, N. Li, C. J. Dolan, Z. J. D. Deng, D. N.
 45 2066–2090. 102 57 Cakan, D. P. Fenning, Y. Yan, M. C. Beard, L. T. Schelhas, A.
 46 40 A. F. Castro-Méndez, F. Jahanbakhshi, D. K. LaFollette, B. 103 Sellinger and J. Huang, *Science (80-)*, 2024, **384**, 1126–
 47 Lawrie, R. Li, C. A. R. Perini, A. M. Rappe and J. P. Correa 104 1134.
 48 Baena, *J. Am. Chem. Soc.*, 2024, **146**, 18459–18469. 105 58 L. Li, Y. Wang, X. Wang, R. Lin, X. Luo, Z. Liu, K. Zhou, S.
 49 41 M. Roß, S. Severin, M. B. Stutz, P. Wagner, H. Köbler, M. 106 58 Xiong, Q. Bao, G. Chen, Y. Tian, Y. Deng, K. Xiao, J. Wu, M. I.
 50 Favin-Lévêque, A. Al-Ashouri, P. Korb, P. Tockhorn, A. 107 Saidaminov, H. Lin, C.-Q. Ma, Z. Zhao, Y. Wu, L. Zhang and
 51 Abate, B. Stannowski, B. Rech and S. Albrecht, *Adv. Energy 108 H. Tan, Nat. Energy*, 2022, **7**, 708–717.
 52 *Mater.*, DOI:10.1002/aenm.202101460. 109 59 Y. Yuan, H. Li, H. Luo, Y. Zhang, X. Li, T. Jiang, Y. Yang, L. Liu,
 53 42 S. D. Öz and S. Olthof, *ACS Appl. Mater. Interfaces*, 110 59 B. Fan and X. Hao, *Energies*, DOI:10.3390/en18102577.
 54 DOI:10.1021/acscami.4c21701. 111 60 M. Liu, L. Bi, W. Jiang, Z. Zeng, S. Tsang, F. R. Lin and A. K.
 55 43 A. Diercks, J. Petry, T. Feeney, R. Singh, T. Zhao, H. Hu, Y. 112 60 -Y. Jen, *Adv. Mater.*, DOI:10.1002/adma.2023044415.
 56 U. W. Paetzold and P. Fassl, *ACS Energy Lett.*, 2025, **11**, 113 61 C. A. R. Perini, A.-F. Castro-Mendez, T. Kodalle, M. Ravello,
 57 1173. 114 61 J. Hidalgo, M. Gomez-Dominguez, R. Li, M. Taddei, R.



- 1 Giridharagopal, J. Pothoof, C. M. Sutter-Fella, D. S. Ginger
2 and J.-P. Correa-Baena, *ACS Energy Lett.*, 2023, **8**, 1408–
3 1415.
- 4 62 M.-G. La-Placa, L. Gil-Escrig, D. Guo, F. Palazon, T. J.
5 Savenije, M. Sessolo and H. J. Bolink, *ACS Energy Lett.*,
6 2019, **4**, 2893–2901.
- 7 63 P. Shi, J. Xu, I. Yavuz, T. Huang, S. Tan, K. Zhao, X. Zhang, Y.
8 Tian, S. Wang, W. Fan, Y. Li, D. Jin, X. Yu, C. Wang, X. Gao,
9 Z. Chen, E. Shi, X. Chen, D. Yang, J. Xue, Y. Yang and R.
10 Wang, *Nat. Commun.*, 2024, **15**, 2579.
- 11 64 M. Rai, L. H. Wong and L. Etgar, *J. Phys. Chem. Lett.*, 2020,
12 **11**, 8189–8194.
- 13 65 P. Mariani, M. Á. Molina-García, J. Barichello, M. I. Zappia,
14 E. Magliano, L. A. Castriotta, L. Gabatel, S. B. Thorat, A. E.
15 Del Rio Castillo, F. Drago, E. Leonardi, S. Pescetelli, L. Vesce,
16 F. Di Giacomo, F. Matteocci, A. Agresti, N. De Giorgi, S.
17 Bellani, A. Di Carlo and F. Bonaccorso, *Nat. Commun.*,
18 2024, **15**, 4552.
- 19 66 J. Borchert, R. L. Milot, J. B. Patel, C. L. Davies, A. D. Wright,
20 L. Martínez Maestro, H. J. Snaith, L. M. Herz and M. B.
21 Johnston, *ACS Energy Lett.*, 2017, **2**, 2799–2804.
- 22 67 T. C.-J. Yang, T. Kang, M. Fitzsimmons, G. Vega, Y. Lu, L.
23 Rosado, A. Jiménez-Solano, L. Pan, S. J. Zelewski, J. Ferrer
24 Orri, Y. Chiang, D. Guo, Z. Y. Ooi, Y. Han, W. Xu, B. Roose, C.
25 Ducati, S. Carretero Palacios, M. Anaya and S. D. Stranks,
26 *EES Sol.*, 2025, **1**, 41–55.
- 27 68 S. Yan, J. B. Patel, J. E. Lee, K. A. Elmetekawy, S. R.
28 Ratnasingham, Q. Yuan, L. M. Herz, N. K. Noel and M. B.
29 Johnston, *ACS Energy Lett.*, 2023, **8**, 4008–4015.
- 30 69 V. Škorjanc, A. Miaskiewicz, M. Roß, S. Maniyarasu, S.
31 Severin, M. R. Leyden, P. Holzhey, F. Ruske, L. Korte and S.
32 Albrecht, *ACS Energy Lett.*, 2024, **9**, 5639–5646.
- 33

View Article Online
DOI: 10.1039/D5EL00193E

Data for this article, including XRD, J-V, EQE, state-of-the-art references on co-evaporated FAPI, are available at ZENODO at <https://doi.org/10.5281/zenodo.17649740>.

Open Access Article. Published on 20 May 2026. Downloaded on 5/21/2026 9:47:14 AM.
This article is licensed under a Creative Commons Attribution 3.0 Unported Licence.

